

Atomic-level insights into CeO₂ performance: Chemical interactions in CMP explored through CeO₂-SiO₂ studies

Ravitej Venkataswamy ^a, Lyle Trimble ^a, Seokgyu Ryu ^a, Ngoc-Tram Le ^a, Kyungju Park ^b, Hyungoo Kang ^b, Jihoon Seo ^{a,*}

^a Department of Chemical and Biomolecular Engineering, Clarkson University, Potsdam, NY, USA

^b C&C Materials Development, SK Hynix Inc., Icheon-si, South Korea



ARTICLE INFO

Handling Editor: Dr P. Vincenzini

Keywords:

Chemical mechanical planarization
Semiconductor
Ceria particles
Surface chemistry
First-principles calculation

ABSTRACT

This study explores the effects of atomic-level factors on the performance of CeO₂ when interacting with SiO₂ films. It specifically examines how different precursors, the ratio of Ce to OH, and reaction temperatures influence outcomes. Our findings reveal that smaller particles, around 5 nm in size, created using a Ce⁴⁺ precursor, are more effective at removing SiO₂ films compared to larger, more crystalline particles from a Ce³⁺ precursor. This is due to their increased interaction with the SiO₂ film during the polishing process, challenging the conventional emphasis on mechanical abrasion in chemical mechanical planarization (CMP) and highlighting the crucial role of chemical interactions. Further analysis through FT-IR and TGA-FTIR techniques showed distinct functional group profiles on the ceria surfaces. Ceria derived from Ce⁴⁺ exhibited a higher presence of OH and NO₃ groups, enhancing adsorption capabilities, as verified by CHN analysis. Importantly, first-principles calculations identified these surface groups as key to improving adhesion to SiO₂ films. Surfaces of amorphous CeO₂, rich in -OH and -NO₃ groups, showed significantly higher adhesion levels than their crystalline counterparts, connecting crystallinity to chemical functionality. This new insight leads to the possibility of designing next-generation CeO₂ abrasives with increased chemical activity.

1. Introduction

The emergence and growth of new technologies, such as autonomous driving, artificial intelligence (AI), 5G communications, the Internet of Things (IoT), and large-scale data processing, have significantly advanced semiconductor technologies [1,2]. To keep pace with these advancing technologies, DRAM and NAND technologies continue to be innovated to achieve higher density, reduced power consumption, and faster speeds beyond the current node [1,2].

Chemical mechanical planarization (CMP) continues to be a critical technology in advancing semiconductor device development, as it aims to achieve high polishing rates, selective removal, uniformity across the wafer and die, and minimal CMP-induced defects and scratches [3–5]. Ceria-based CMP slurries have been widely used for polishing various types of SiO₂, Si₃N₄, and other related dielectric films due to their high oxide removal rates (RRs) and selectivity, particularly in the formation of shallow trench isolation (STI) structures [6–9]. Recent advancements in particle technology have driven innovation in ceria-based CMP slurry

development, enabling the fabrication of smaller geometries and complex schemes. However, as feature sizes continue to shrink, reducing the formation of scratches and defects on wafer surfaces during polishing remains a challenge. There is currently a significant demand for ceria particles that are smaller than 10 nm [10], as they have the potential to meet the highly demanding new requirements for defect reduction. These smaller ceria particles are known as superfine CeO₂ particles.

Only a few papers have reported on the synthesis of superfine CeO₂ particles for CMP applications [11,12]. The approach taken by the published papers involves preparing Ce(OH)₄ particles that are less than 10 nm in diameter, which differs significantly from the traditional approach used to prepare well-crystalline CeO₂ particles for SiO₂ CMP. The degree of crystallinity and particle size of ceria are known to affect the oxide removal rate. However, it has been observed that despite having relatively low degrees of crystallinity, Ce(OH)₄ particles demonstrate a high rate of SiO₂ film removal. T. Iwano et al. reported that superfine ceria particles containing Ce(OH)_aX_b (X = NO₃⁻ and SO₄²⁻) [11], in which the anions can activate a Ce atom to improve the

* Corresponding author.

E-mail address: jseo@clarkson.edu (J. Seo).

reactivity of $\text{Ce}(\text{OH})_4$ particles, lead to higher SiO_2 RRs. Later, Y. Son et al. suggested that the larger total contact area of smaller $\text{Ce}(\text{OH})_4$ particles during polishing results in a higher SiO_2 film polishing rate [12], which was referred to as the contact-area-based CMP mechanism. Despite the aforementioned studies, the fundamental reasons behind the high oxide removal rate observed in superfine CeO_2 particles with low crystallinity remain unclear. Gaining insight into this matter is important, given the substantial investments of time and effort still being made in the utilization of smaller and highly crystalline CeO_2 particles.

Superfine CeO_2 particles are typically synthesized through the precipitation method [11,12], which involves preparing Ce precursors, followed by their precipitation through -OH group reactions and transformation into CeO_2 particles. Although this method is simple, cost-effective, and easily scalable, the physicochemical properties of the resulting particles can be affected by various synthesis parameters, including pH, temperature, additives, and the types and concentrations of reactants [13,14]. Our hypothesis is that a combination of these parameters plays a crucial role in determining the properties of superfine ceria particles, including their polishing behaviors. Key synthesis parameters can influence the crystallization process, including nanocrystal nucleation, growth, and aggregation into $\text{Ce}(\text{OH})_4$ and/or CeO_2 crystals, as well as the rate of dissolution of non-stable structures [11–14].

In this study, we investigated how various parameters, including the types of Ce precursors, the concentration of the precipitation agents, reaction pH, and temperature, impact the properties of superfine CeO_2 particles and their polishing behaviors. To gain a deeper understanding of the mechanism underlying SiO_2 film removal by superfine CeO_2 particles, we conducted computational simulations based on density functional theory (DFT). Gaining a comprehensive understanding of superfine CeO_2 particles and their impact on CMP performance is crucial for optimizing synthesis techniques and offering direction in designing and producing superfine CeO_2 particles for advanced device CMP applications.

2. Experimental

2.1. Materials

Cerium (III) nitrate hexahydrate ($\text{Ce}(\text{NO}_3)_3 \cdot 6\text{H}_2\text{O}$), ammonium cerium (IV) nitrate ($(\text{NH}_4)_2\text{Ce}(\text{NO}_3)_6$), and ammonium hydroxide (NH_4OH) were sourced from Sigma Aldrich. Polyvinyl alcohol (PVA) was acquired from Polysciences, Inc. Additionally, 2000 nm-thick oxide films, which were deposited on 200 mm diameter Si wafers using plasma-enhanced chemical vapor deposition with tetraethyl orthosilicate (PETEOS), were procured from DK Nanotechnology.

2.2. Preparation of superfine CeO_2 particles and the slurry preparation

Superfine ceria particles were synthesized using $\text{Ce}(\text{NO}_3)_3$ and $(\text{NH}_4)_2\text{Ce}(\text{NO}_3)_6$ as precursors for Ce^{3+} and Ce^{4+} ions, respectively. This was achieved through a precipitation method at room temperature (RT) and 80 °C. We prepared solutions of 0.1 M $\text{Ce}(\text{NO}_3)_3$ and 0.1 M $(\text{NH}_4)_2\text{Ce}(\text{NO}_3)_6$ in deionized (DI) water, which were then mixed with NH_4OH . This resulted in the formation of superfine ceria particles. NH_4OH was incrementally added to the solution, maintaining varying molar ratios of Ce ion to OH^- (1:1, 1:2, 1:3, 1:4, and 1:5). The initial phase of the reaction was conducted at RT for 12 h, following which the particles were collected. To explore the effects of temperature, the reaction temperature was then increased to 80 °C, and the process was continued for an additional 6 h. No significant changes were observed when stirring was extended beyond this duration. The synthesized particles were then washed with DI water and centrifuged until their conductivity was reduced to less than 1.5 $\mu\text{S}/\text{cm}$, ensuring the removal of residual ions.

For slurry preparation, the synthesized particles were dispersed in DI water at a concentration of 0.2 wt%. Additionally, 0.2 wt% PVA was added as a stabilizing agent. The pH of the slurries was then adjusted to 6

using either HNO_3 or KOH.

2.3. Material characterization

The X-ray diffraction (XRD) patterns of the ceria particles were examined using a Bruker D8 Advance instrument. For identifying the surface functional groups of these particles, Fourier transform infrared (FT-IR) spectroscopy was performed utilizing the Nicolet iS10 from Thermo Scientific. Also, Thermogravimetry analysis (TGA) was coupled with FT-IR for continuous evolved gas analysis. This was conducted at a heating rate of 10 °C/min in a nitrogen atmosphere, using a Nicolet iS50 equipped with a derivative thermogravimetry detector and an IR cell, also from Thermo Fisher Scientific. TGA-FTIR measurements were taken up to 700 °C, and the FT-IR spectra were analyzed using OMNIC software.

The CHN contents in the as-synthesized ceria particles were quantified using an elemental analyzer (Model 2400(II)) from PerkinElmer. Absorbance spectra were recorded with a UV-visible spectrometer (Lambda 35, PerkinElmer) in the 200–500 nm wavelength range, with samples placed in a 1.0 cm long quartz cuvette. Additionally, Raman spectroscopy was employed to examine the ceria particles using a Nicolet DXR Raman Microscope from Thermo Scientific. This analysis spanned a wavelength range of 400–1600 nm, with the samples prepared as solid dried powders on a glass slide.

The morphological characterization (shape and size distribution) of ceria particles was performed using a transmission electron microscope (TEM, JEM-2010). High-resolution spectra of Ce 3d and O 1s for the synthesized ceria particles were acquired through X-ray photoelectron spectroscopy (XPS) at the Cornell Center for Materials Research. The data from this analysis was processed using XPSPEAK-4.1 software.

2.4. Chemical mechanical planarization

The 8-inch blank SiO_2 wafers were polished for 1 min using a POLI-500 polisher from G&P Technology at 93/87 rpm platen/carrier speed, 3 psi down-pressure, and a slurry flow rate of 150 ml/min. The IC-1000 Dupont polishing pad was conditioned *ex-situ* with a 3M A63 diamond conditioner. The thickness of the films was determined by measuring them with an interferometer (FilmTek 2000, Bruker) before and after polishing at 48 points across the diameter of the 200 mm wafer. This process was repeated with two different wafers to ensure accuracy, and the average values of these measurements are presented in this report.

2.5. Computational details

DFT as implemented in the Vienna ab initio simulation package (VASP) was used to conduct first-principles calculations [15]. We employed a spin-polarized DFT + U methodology [16], adopting a Hubbard parameter of 5.0 eV to accurately describe the nature of the 4f electrons of Ce. Additionally, we incorporated the dispersion correction (DFT-D2) proposed by Grimme [17] to address the long-range van der Waals interactions.

In our calculations, we used a plane wave basis set, setting the cut-off energy at 450 eV. To address both core and valence electrons, the Projector Augmented Wave (PAW) method was employed. For the exchange-correlation function, our approach involved the use of the Generalized Gradient Approximation (GGA), specifically following the formulation by Perdew, Burke, and Ernzerhof (PBE).

The amorphous CeO_2 model structure was derived from its crystalline form using a melt-quenching technique, a process part of our ab initio molecular dynamics (AIMD) simulations. We used a $4 \times 4 \times 1$ supercell of the crystalline CeO_2 structure, which was annealed at a high temperature of 5000 K for 5 ps using a time step of 1 fs. To enable local structural rearrangements, the initial structure was expanded to 110 % of its original ground state volume. Subsequently, the samples underwent a rapid quenching process to a temperature of 298 K at a cooling

rate of 2.0 K/fs. This step was followed by both volume and geometric optimization. For the AIMD simulations, the Brillouin zone sampling was confined to the gamma point. However, for static energy calculations, a denser k-point mesh of $2 \times 2 \times 1$, as per the Monkhorst-Pack scheme [18], was utilized.

For the calculation of surface interactions between CeO_2 and SiO_2 , a $4 \times 4 \times 1$ k-point grid was utilized for integrations across the Brillouin zone. The dimensions of the supercell were set to an $11.5 \text{ \AA} \times 13.3 \text{ \AA} \times 32.3 \text{ \AA}$. The cutoff energy for the plane wave was set at 450 eV in the reciprocal area, with a smearing width of 0.2 eV. Furthermore, the convergence criterion for the self-consistent field was set at 10^{-5} eV. To determine the Ce-O-Si bonding distance between CeO_2 and SiO_2 , energy calculations were based on a structure achieved through sufficient thermodynamic stabilization. In this study, all supercell models were transformed into crystallographic data using the VESTA software (version 3.5.8). The conversion process utilized CONTCAR files, which were obtained from DFT calculations.

3. Results and discussion

3.1. Impact of types of Ce precursors (Ce^{3+} and Ce^{4+}), concentrations of precipitation agents, and the reaction temperature on the physicochemical properties of superfine ceria particles

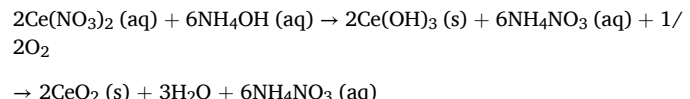
Fig. 1 presents the XRD results of superfine ceria particles synthesized using $\text{Ce}(\text{NO}_3)_3$ and $(\text{NH}_4)_2\text{Ce}(\text{NO}_3)_6$ as Ce^{3+} and Ce^{4+} precursors, respectively. These particles were prepared with varying molar ratios of Ce precursors to the precipitating agent, ranging from 1:1 to 1:5, at both RT and 80 °C. The XRD patterns reveal that all as-synthesized samples exhibit peaks consistent with the face-centered cubic CeO_2 structure (JCPDS-34-0394). Notably, superfine ceria particles derived from $\text{Ce}(\text{NO}_3)_3$ (**Fig. 1a**) demonstrate significantly higher crystallinity compared to those synthesized from $(\text{NH}_4)_2\text{Ce}(\text{NO}_3)_6$ (**Fig. 1b**), irrespective of the reaction temperature. This suggests that the type of Ce precursors has a marked influence on the crystallinity of CeO_2 .

Table I summarizes the crystallite size (d_{XRD}), lattice parameter, and crystallinity values for two sets of superfine ceria particles, calculated from **Fig. 1**. Overall, samples prepared with the Ce^{3+} precursor exhibit larger crystallite sizes than those prepared with the Ce^{4+} precursor. Specifically, ceria particles synthesized with the Ce^{3+} precursor have a d_{XRD} range of 6.8–13.5 nm, whereas those synthesized with the Ce^{4+} precursor range from 4.9 nm to 6.6 nm across both temperature conditions (**Table I**). The TEM images of the ceria particles are shown in **Fig. S2**. These images reveal that the particle sizes are consistent with the crystalline sizes, indicating that the particles are primarily composed of single crystals. Furthermore, the crystallinity of the ceria particles also varies depending on the precursors and the Ce/OH ratio, with

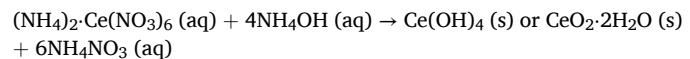
samples prepared with Ce^{3+} precursor exhibiting higher crystallinity ($85 \pm 1 \%$) compared to those prepared with Ce^{4+} precursor ($64 \pm 1 \%$) (**Table I**).

The question arises as to why the crystallite size and crystallinity values significantly differ based on the chosen precursors and the Ce/OH ratio in the synthesis of superfine ceria particles. As described in the experimental section, 0.1 M solutions of $\text{Ce}(\text{NO}_3)_3$ and $(\text{NH}_4)_2\text{Ce}(\text{NO}_3)_6$ were prepared in DI water and mixed with NH_4OH in varying molar ratios of Ce ion to OH⁻ to prepare the superfine ceria particles.

For the samples derived from the Ce^{3+} precursor, the addition of NH_4OH to the $\text{Ce}(\text{NO}_3)_3$ solution resulted in a noticeable color change (**Fig. S1**). Initially, the solution transitioned from colorless to dark gray and finally settled into a pale yellow (**Fig. S1**). This color change with $\text{Ce}(\text{NO}_3)_3$ is likely due to precipitation followed by dehydration/oxidation reactions, which are influenced by dissolved oxygen in the solution and at the air-liquid interface [14]. Dark gray $\text{Ce}(\text{OH})_3$ precipitates form as Ce^{3+} ions react with NH_4OH [14]. In the air, $\text{Ce}(\text{OH})_3$ is unstable and oxidizes to CeO_2 when stirred vigorously in the presence of O_2 [14].



In the case of the samples derived from the Ce^{4+} precursor, the addition of NH_4OH to the transparent orange $(\text{NH}_4)_2\text{Ce}(\text{NO}_3)_6$ solution resulted in a precipitation reaction, forming yellow $\text{Ce}(\text{OH})_4$ (**Fig. S1**). The color of the precipitate remained constant throughout the subsequent dehydration process (**Fig. S1**), which converts $\text{Ce}(\text{OH})_4$ to $\text{CeO}_2 \cdot 2\text{H}_2\text{O}$. This consistency in color is indicative of the fact that the oxidation state of Ce does not change during this transformation.



The distinct color changes and chemical behaviors observed in the CeO_2 particles synthesized from Ce^{3+} and Ce^{4+} precursors [14] suggest that the initial oxidation state of Ce and the specific reaction pathway have a significant impact on the final properties of the superfine ceria particles. The nucleation and growth of CeO_2 particles in the precursor solution are critical stages that are significantly influenced by various synthesis conditions such as the concentration of the cerium precursors, precipitants, reaction temperature, and process duration [13]. Our experiments, conducted at both RT and 80 °C with varying molar ratios of Ce precursor to -OH, indicate that the type of Ce precursors is an important factor in defining the crystalline quality of CeO_2 particles, as shown in **Fig. 1**. Higher crystal quality is typically associated with slower nucleation rates, allowing more time for particle growth [19–21]. This slow growth enables particles to develop a more orderly and

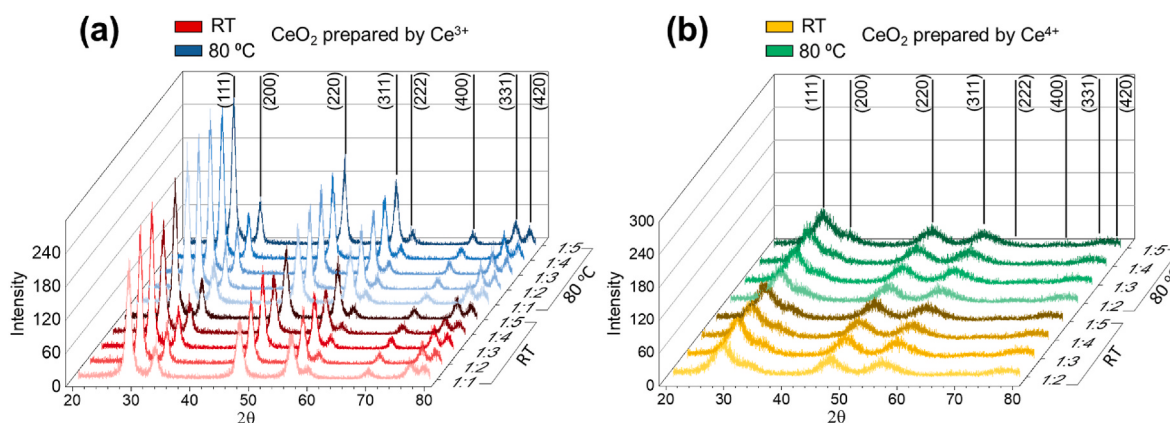


Fig. 1. XRD patterns of superfine ceria particles synthesized using (a) $\text{Ce}(\text{NO}_3)_3$ and (b) $(\text{NH}_4)_2\text{Ce}(\text{NO}_3)_6$ as Ce^{3+} and Ce^{4+} precursors, respectively, at both RT and 80 °C with varying molar ratios of Ce precursor to -OH. Note: No precipitation at a 1:1 M ratio of Ce^{4+} to -OH.

Table 1

Crystallite size (d_{XRD}), lattice parameter, and crystallinity values for superfine ceria particles synthesized using $\text{Ce}(\text{NO}_3)_3$ and $(\text{NH}_4)_2\text{Ce}(\text{NO}_3)_6$ as Ce^{3+} and Ce^{4+} precursors, respectively.

Ce precursor/ OH^-	$\text{Ce}^{3+}/\text{OH}^-$					$\text{Ce}^{4+}/\text{OH}^-$				
	1:1	1:2	1:3	1:4	1:5	1:1	1:2	1:3	1:4	1:5
d_{XRD} (nm)	6.8	9.0	9.6	8.2	9.1	—	4.9	4.8	4.9	6.6
d_{XRD} (nm) prepared at 80 °C	7.2	13.5	12.6	11.6	11.6	—	5.2	5.3	4.0	5.5
Lattice Parameter (nm)	0.54	0.54	0.54	0.54	0.54	—	0.54	0.54	0.54	0.54
Lattice Parameter (nm) prepared at 80 °C	0.54	0.54	0.54	0.54	0.54	—	0.54	0.54	0.54	0.54
Crystallinity (%)	83	85	85	84	85	—	63	65	65	64
Crystallinity (%) prepared at 80 °C	85	86	86	86	86	—	64	64	64	64

well-defined crystal structure, thereby enhancing crystallinity. In contrast, rapid growth, indicative of faster nucleation rates, may not provide sufficient time for particles to properly arrange themselves, leading to a less organized structure and lower crystallinity.

According to classical nucleation theory [19], the degree of supersaturation is a key factor in determining the nucleation rate. Supersaturation is especially critical as high levels can lead to the formation of non-equilibrium phases or amorphous regions, reducing crystal quality [19]. The relationship between the solubility of Ce precursors and supersaturation can be described mathematically. For instance, the solubility of different Ce ion species in water is given by the equations: $S = [\text{Ce}^{3+}][\text{OH}^-]/K_{sp}$ and $S = [\text{Ce}^{4+}][\text{OH}^-]/K_{sp}$ where S represents supersaturation and K_{sp} is the solubility constant for $\text{Ce}(\text{OH})_3$ and $\text{Ce}(\text{OH})_4$ respectively. The solubility of Ce^{3+} ions ($K_{sp} = 1.6 \times 10^{-20}$) is significantly higher than that of Ce^{4+} ions ($K_{sp} = 2 \times 10^{-48}$) [22]. This higher solubility and surface energy of smaller $\text{Ce}(\text{OH})_3$ particles, present during the synthesis of superfine ceria particles from Ce^{3+} ions, lead to their redissolution and subsequent incorporation into well-structured ceria particles. Conversely, the very low solubility of Ce^{4+} solutions may contribute to reduced crystallinity due to higher supersaturation and a faster nucleation rate associated with Ce^{4+} .

3.1.1. SiO_2 film removal rates using CeO_2 -based CMP slurries

Fig. 2 presents a comparative analysis of the removal rates of SiO_2 films using CeO_2 -based CMP slurries, prepared with Ce^{3+} and Ce^{4+} precursors under varying OH molar ratios and temperatures. A key

observation from this data is that slurries synthesized from the Ce^{4+} precursor demonstrate higher removal rates compared to those derived from the Ce^{3+} precursor. It is well-understood in CMP processes that larger particles typically contribute to higher removal rates due to their mechanical abrasive action, whereas smaller particles facilitate removal primarily through chemical action. In our study, despite the smaller size (5 nm) of Ce^{4+} -derived superfine particles, they exhibit a higher removal rate than those derived from the Ce^{3+} precursor. This observation highlights the significant role of chemical action, possibly influenced by the surface chemistries present on the superfine ceria particles.

3.1.2. Surface chemistry of Ce^{3+} and Ce^{4+} -derived CeO_2 particles

FT-IR spectra of superfine CeO_2 particles synthesized using Ce^{3+} and Ce^{4+} precursors are shown in Fig. 3. Notable peaks in the 500–700, 1025, 1380, and 1425 cm^{-1} regions correspond to Ce-O stretching vibrations, Ce-O-Ce stretching bands [23], -NO₃ species [7], and NH₄⁺ species, respectively. A band at 1630 cm^{-1} is related to the bending mode of H₂O. The -OH stretching bands of all superfine ceria particles are detected in the range of 3200–3600 cm^{-1} (data not shown).

Significant differences in adsorption characteristics are observed between Ce^{3+} and Ce^{4+} -derived superfine ceria particles, particularly in the absorption peaks associated with -NO₃ species on ceria surfaces. The -NO₃ species peak in the particles from Ce^{3+} reduces as the molar ratio of Ce ions to OH⁻ increases (Fig. 3a), disappearing entirely beyond a Ce^{3+} to OH⁻ molar ratio of 1:2. It is known that -NO₃ groups gradually decrease as the reaction pH increases, being fully replaced by OH groups at a pH above 10.5. Interestingly, all superfine ceria particles generated from Ce^{4+} show a -NO₃ species peak (Fig. 3b), even though they were prepared under alkaline conditions, indicating an enhanced adsorption capacity for -NO₃ species. Compared to -OH concentration and reaction pH, the reaction temperature has a relatively minor effect on the adsorption of -NO₃ species on ceria surfaces under the conditions we were interested in.

Anionic species such as OH⁻ and NO₃⁻ can interact with surface Ce sites through electrostatic and coordination bonds. Both Ce sites (Ce^{3+} and Ce^{4+}) on ceria surfaces can act as Lewis acids, accepting electron pairs from Lewis bases such as OH⁻ and NO₃⁻ species [25–27]. The amorphous regions in ceria particles with low crystallinity, prepared by Ce^{4+} , can increase the number of surface acidic sites. These include Ce³⁺ sites and O vacancies, potentially enhancing the adsorption of -NO₃ species on the ceria surface during particle synthesis. The amorphous region has non-ideal coordination numbers between Ce and O atoms, while the crystalline region has Ce and O coordination numbers of 8 and 4, respectively. The less organized structure and reduced crystallinity of superfine ceria, derived from Ce^{4+} compared to Ce^{3+} , likely lead to an increased number of Lewis acid sites. This increase promotes interactions with anionic species like OH⁻ and NO₃⁻. As a result, superfine ceria particles with low crystallinity originating from Ce^{4+} show higher adsorption capacities for NO₃⁻ species.

Our findings from XRD, FT-IR, and CMP results consistently demonstrate that the selection of Ce precursors plays a crucial role in the formation of superfine ceria particles and significantly influences their

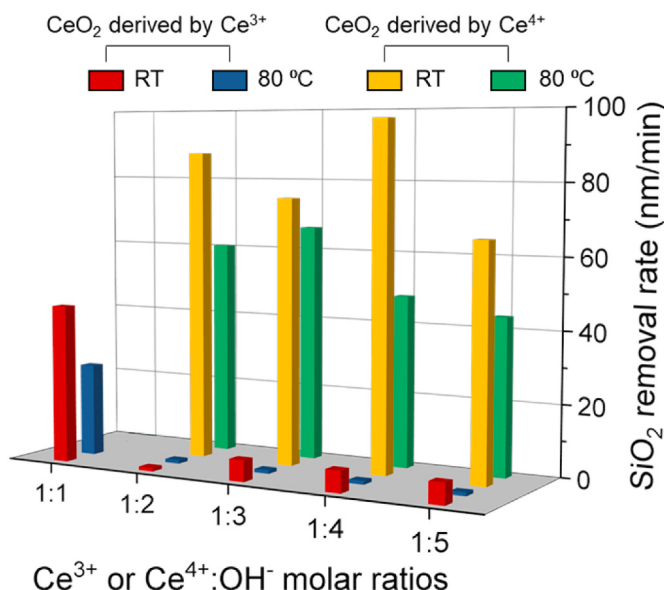


Fig. 2. SiO_2 film removal rates using slurry comprising 0.2 wt% CeO_2 particles derived from Ce^{3+} and Ce^{4+} precursors with varying molar ratios of Ce precursor to -OH. Note: The slurries were adjusted to pH 6.0. There was no precipitation at a 1:1 M ratio of Ce^{4+} to -OH.

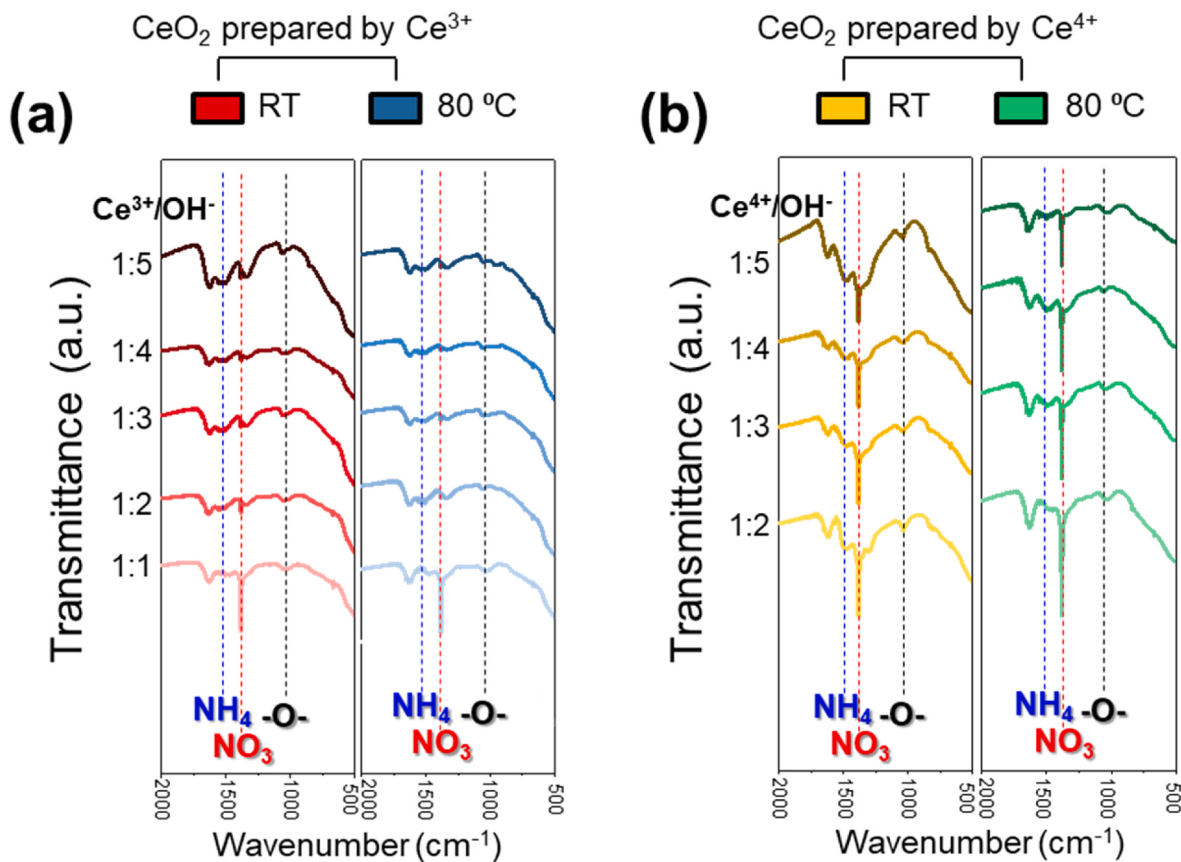


Fig. 3. FT-IR spectra of CeO₂ particles derived from (a) Ce³⁺ and (b) Ce⁴⁺ precursors with varying molar ratios of Cerium ion to OH⁻ at both RT and 80 °C in the region of 500–2000 cm⁻¹.

CMP performances. To focus our research more effectively, we concentrated exclusively on studying superfine ceria samples prepared using a molar ratio of 1:2 for both Ce³⁺ to OH⁻ and Ce⁴⁺ to OH⁻.

Fig. 4a and b shows 3D in-situ IR spectra, capturing the evolving gas emissions from ceria across a temperature range of 50–700 °C. Initially, minor peaks appear in the absorption bands from 3500 to 3960 cm⁻¹ at 50 °C [28,29], which are accompanied by bands between 2300 and 2400 cm⁻¹ [28,29]. These bands are attributed to water vapor and CO₂, respectively, and are observed consistently throughout the examined temperature range. Notably, The peak associated with CO₂ increases in intensity over the temperature spectrum, reaching its highest peak around 270 °C before decreasing again. The presence of CO₂ formation suggests that it may either originate from the surrounding atmosphere or result from the oxidation and/or decomposition of hydrocarbon impurities on the ceria particles. Elemental analysis supports this assumption, revealing carbon concentrations of 0.65 % and 0.61 % in ceria particles derived from Ce³⁺ and Ce⁴⁺, respectively, as indicated in Table 2.

New peaks at 1598 and 1630 cm⁻¹, observed at 300 °C in the Ce⁴⁺-derived ceria particles (Fig. 4c), are associated with the formation of nitric dioxide (NO₂) from the ceria surface [30,31]. This formation is a result of the decomposition of the NO₃ group (Fig. 3b). The TG analysis profile (Fig. 4d) indicates that Ce⁴⁺-derived ceria particles have 11 % weight loss, which is significantly higher than the 3 % loss in Ce³⁺-derived particles, possibly due to higher densities of the surface functional group.

The surface functional group densities of superfine ceria particles were determined through CHN analysis. Up to temperatures of 700 °C, the gases evolved from the surface consisting only of H₂O, CO₂, and NO₂, as shown in Fig. 4a–c. The densities of their surface functional groups were calculated under the assumption that they are composed exclusively of groups related to H, C, and N (e.g., OH, CH₃, NO₃), as shown in

Figs. 3 and 4. Initially, H was considered for CH₃ based on the concentration of C, and any remaining H was presumed to contribute to OH. Ce³⁺-derived CeO₂ particles contained 0.61 % C and 0.23 % H with surface densities of 3.52 nm² for CH₃ groups and 15.91 nm² for OH groups. In contrast, Ce⁴⁺-derived CeO₂ particles had 0.65 % C, 0.62 % H, and 1.34 % N, with surface densities of 2.10 nm² for CH₃ groups, 24.08 nm² for OH groups, and 3.72 nm² for NO₃ groups. The presence of CH₃ groups in the CeO₂ particles could be attributed to impurities during their synthesis, as similar concentrations were found in both types of ceria particles. The higher density of OH groups on the Ce⁴⁺-derived CeO₂ particles, along with the presence of NO₃ groups, might be one of the reasons for the higher SiO₂ removal rates seen with Ce⁴⁺-derived CeO₂ particles.

The surface Ce³⁺ ions of CeO₂ particles are known to be highly reactive [32–34], playing a crucial role in achieving high removal rates of SiO₂ films during CMP. To assess this, UV-vis spectra of CeO₂ particles prepared using two different precursors were analyzed to evaluate the oxygen-metal ion charge-transfer bands of CeO₂ particles, as illustrated in Fig. 5a. CeO₂ particles exhibit two absorption peaks centered at 255 and 285 nm, which correspond to O²⁻ → Ce³⁺ and O²⁻ → Ce⁴⁺ charge-transfer [35], respectively. Notably, CeO₂ particles prepared with the Ce⁴⁺ precursor show a higher absorption peak at 255 nm (Fig. 5a), indicating a higher surface concentration of Ce³⁺ ions.

When an oxygen vacancy (O_v) is created in the lattice, it typically leaves behind two electrons, often resulting in the formation of two Ce³⁺ ions near the vacancy. The amorphous phase of CeO₂ tends to form O_v more readily, with a lower formation energy of 1.70 eV [36], compared to crystalline CeO₂ (3.32 eV). Consequently, the low crystalline phase of CeO₂ can exhibit a higher concentration of Ce³⁺ ions on its surface, characterized by a lower surface energy of 0.92 J/m² and a lower surface oxygen vacancy formation energy of 1.20 eV [36].

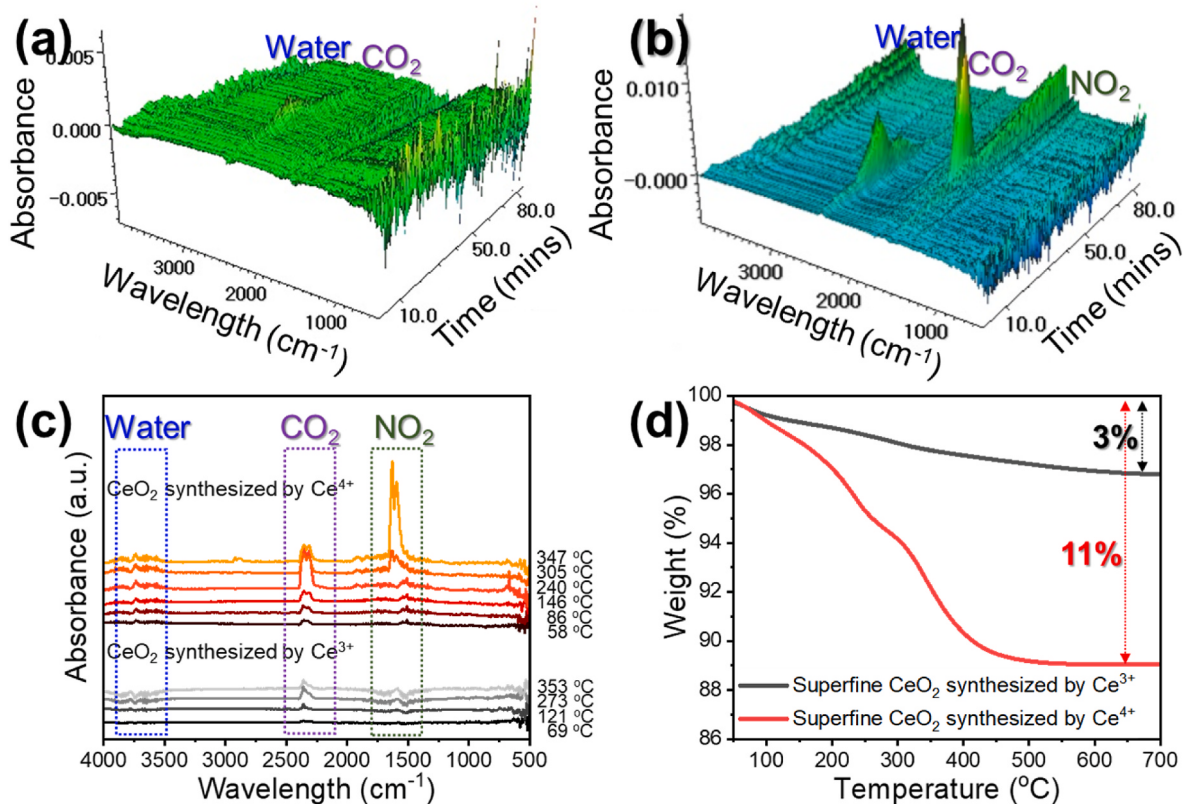


Fig. 4. In situ 3D image of IR spectra of the evolving gas emissions from (a) Ce^{3+} and (b) Ce^{4+} -derived CeO_2 particles within the temperature range of 50–700 °C. (c) A comparison of the in-situ individual spectra of TGA exhaust gas from CeO_2 particles and their (d) TGA profiles.

Table II

Elemental composition of superfine ceria particles and their associated functional groups. The surface densities of CH_3 , OH , and NO_3 groups were determined using the element contents from CHN analysis. The calculation formula is Functional groups $\text{nm}^{-2} = a \times N_A / (M \times S \times 10^{20})$ where a (%) represents the elemental content derived from CHN analysis, N_A is Avogadro's number (6.02×10^{23}), M is the molar mass of the total elements in the respective functional group, and $S = 6d^2/(dp)$ where d is the average particle size, which is 10 nm for Ce^{3+} -driven CeO_2 and 5 nm for Ce^{4+} -driven CeO_2 , respectively. The ρ represents the bulk density of CeO_2 , which is 7.65 cm^{-3} .

	Elemental analysis (%)			Densities of functional groups (nm^{-2}) ^a			Weight loss (wt%)	
	C	H	N	CH_3	OH	NO_3	w ^b	w (T ₇₀₀) ^c
Ce^{3+} -driven CeO_2	0.61	0.23	0	3.52	15.91	0.00	4	3
Ce^{4+} -driven CeO_2	0.65	0.62	1.34	2.10	24.08	3.72	12	11

^a The surface density calculation is based on the C, H, and N contents from CHN analysis. Although NH_4^+ was observed, it is not considered in CHN analysis due to its negligible quantity compared to other groups.

^b Weight percentage is calculated from elemental analysis, assuming the formation of CO_2 , H_2O , and NO_2 .

^c Weight percentage as determined in TG analysis at 700 °C.

Fig. 5b presents the Raman spectra of CeO_2 particles synthesized using the two different precursors. A dominant peak at 464 cm^{-1} (F_{2g}) relates to the positions of oxygen atoms around the Ce ions and is sensitive to crystal symmetry [37]. Both CeO_2 particles exhibit a stronger Raman peak around 460 cm^{-1} , attributed to the F_{2g} vibration mode of the CeO_2 lattice. In ceria particles synthesized with Ce^{4+} , the F_{2g} Raman mode shifts the peak at 460 cm^{-1} downwards as the cell parameter increases [38]. They also show a strong Raman peak around 600 cm^{-1} ,

indicative of the presence of O_v [37]. The Raman results suggest that O_v is more prevalent in CeO_2 particles with low crystallinity, which is correlated with our observation in **Fig. 1** and Table I. A peak at 750 cm^{-1} is attributed to NO_3^- ions in inner-sphere complexes [39]. The band around 1045 cm^{-1} is ascribed to bound NO_3^- ions [39]. Bidentate nitrates ($1556\text{--}1605 \text{ cm}^{-1}$) on the ceria surface prepared with Ce^{4+} are indicated by their presence [39], while no NO_3^- spectra are observed on surfaces prepared with Ce^{3+} . This difference in spectral features highlights the variance in surface chemistry based on the precursor used in the synthesis of CeO_2 particles.

The concentration ratios of $\text{Ce}^{3+}/\text{Ce}^{4+}$ in two different types of CeO_2 particles were determined using the $\text{Ce } 3d_{5/2}$ and $\text{Ce } 3d_{3/2}$ XPS spectra, as shown in **Fig. 6a**. To calculate the Ce^{3+} concentration on the ceria surface, the XPS spectra were deconvoluted into ten peaks using a mixed Gaussian–Lorentzian function model. **Table 3** presents the binding energies (BE) and the relative area ratios of these peaks for the ceria particles. In this table, the v and u labels correspond to the $\text{Ce } 3d_{5/2}$ and $\text{Ce } 3d_{3/2}$ spectra, respectively. Peaks v_0 , v_1 , u_0 and u_1 are attributed to Ce^{3+} (red region in **Fig. 6a**), while peaks v , v_2 , v_3 , u , u_2 , and u_3 are indicative of Ce^{4+} (blue region in **Fig. 6b**) [40,41]. The relative surface concentration of Ce^{3+} was calculated from the total integrated area of the v_0 , v_1 , u_0 and u_1 peaks. As **Table 3** shows, Ce^{4+} -derived CeO_2 particles exhibited a significantly higher Ce^{3+} concentration (24.2 %) compared to those synthesized using Ce^{3+} (20 %). This difference is attributed to the lower O_v formation energy in particles with reduced crystallinity.

Additionally, the O1s spectra shown in **Fig. 6b** were analyzed by fitting the spectrum at three distinct binding energies: 530.2 eV (blue region), 531.4 eV (red region), and 533.3 eV (dashed red region). 530.2 eV and 531.4 eV represent lattice oxygen (O_L) and O_v [42,43], respectively, while the peak at 533.3 eV corresponds to chemisorbed species such as nitrates, hydroxyls, and/or water molecules associated with Ce^{3+} [44–46]. Not surprisingly, XPS survey scans indicated a significant N peak in Ce^{4+} -derived CeO_2 particles (data not shown). Although CeO_2

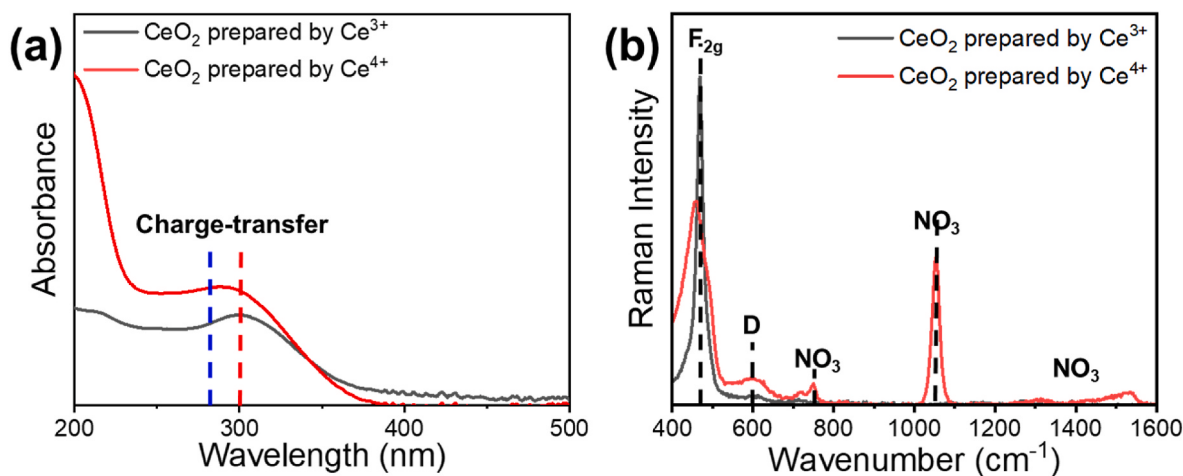


Fig. 5. (a) UV-vis and (b) Raman spectra of superfine CeO₂ particles synthesized by Ce³⁺ and Ce⁴⁺ precursors.

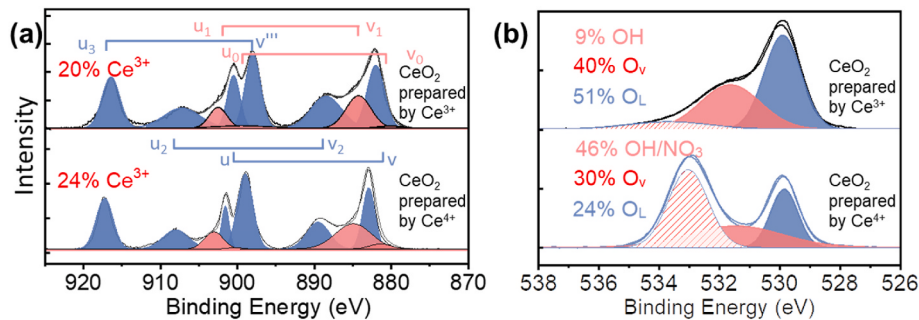


Fig. 6. (a) Ce3d and (b) O1s XPS spectra of superfine CeO₂ particles synthesized by Ce³⁺ and (b) Ce⁴⁺ precursors at RT. Blue regions symbolize Ce⁴⁺ species, while red regions denote Ce³⁺ species. (For interpretation of the references to color in this figure legend, the reader is referred to the Web version of this article.)

Table III

XPS binding energies (eV) and relative area ratios (%) of individual peaks of Ce 3d for superfine CeO₂ particles synthesized by Ce³⁺ and Ce⁴⁺ precursors at RT.

Peak assignment	Ce 3d5/2					Ce 3d3/2					Ce ³⁺ (%)	
	ν_0	ν	ν_1	ν_2	ν_3	u_0	u	u_1	u_2	u_3		
	Ce ³⁺	Ce ⁴⁺	Ce ³⁺	Ce ⁴⁺	Ce ⁴⁺	Ce ³⁺	Ce ⁴⁺	Ce ³⁺	Ce ⁴⁺	Ce ⁴⁺		
CeO ₂ prepared by Ce ³⁺	B. E. (eV)	880.2	882.1	884.2	888.5	898.0	899.4	900.6	902.3	907	916.5	20.0
CeO ₂ prepared by Ce ³⁺	Peak area (%)	0.75	16.1	12.4	13.6	16.4	1.1	9	7.4	9.8	13.3	
CeO ₂ prepared by Ce ⁴⁺	B. E. (eV)	880.4	882.0	884.0	888.6	898.0	899.4	900.6	902.1	907	916.3	24.2
CeO ₂ prepared by Ce ⁴⁺	Peak area (%)	1.94	13.6	16.1	11	21	0.35	5.9	5.8	9	15.3	

particles with low crystallinity synthesized by Ce⁴⁺ display a higher Ce³⁺ concentration than those produced using Ce³⁺ (Fig. 1), most of the Ce³⁺ sites in the Ce⁴⁺-derived particles are bound to -OH and -NO₃ on the ceria surface. This observation draws attention to the importance of understanding how the functional groups present on the ceria surface impact their interaction with SiO₂. This understanding is crucial for comprehending the overall CMP performance of these superfine CeO₂ particles.

3.1.3. Interfacial adhesion properties of SiO₂ on crystalline and amorphous CeO₂ surfaces

The functional groups present in CeO₂ particles derived from Ce³⁺ and Ce⁴⁺ precursors show notable differences, which significantly affect how they interact with SiO₂ surfaces during the CMP process. To better understand these interactions, we conducted a theoretical study examining the interfacial adhesion properties of CeO₂ surfaces. Our research concentrated on various species observed, including the O_L, O_v, -OH groups, and -NO₃ groups on the ceria surface. We focused specifically on

examining amorphous structures, rather than less organized forms, and compared their properties to those of crystalline structures.

Fig. 7 shows the adhesion work (W_{ad}) at the interfaces between SiO₂ and two different CeO₂ surfaces: the crystalline (cCeO₂) and the amorphous (aCeO₂) forms, each with various surface functional groups such as O_L, O_v, -OH groups, and -NO₃ groups. W_{ad} quantifies the bond strength between two surfaces. It is calculated by subtracting the total energy of the individual materials (E_{SiO_2} and E_{CeO_2}) from the combined interface energy (E_{SiO_2/CeO_2}) and then dividing this difference by the contact area (A), as per the formula: $W_{ad} = (E_{SiO_2} + E_{CeO_2} - E_{SiO_2/CeO_2}) / A$. Here, E_{SiO_2} and E_{CeO_2} are the energies of the individual supercell slabs, while E_{SiO_2/CeO_2} represents the total energy when a Ce-O-Si bond forms between the SiO₂ and CeO₂ interfaces.

According to Fig. 7a, the W_{ad} values for interfaces between SiO₂ and cCeO₂-O_L and -OH groups (cCeO₂-OH) are 0.50 J/m². The presence of O_v increases this value to 0.58 J/m², suggesting a stronger bond with SiO₂ due to the high reactivity from these vacancies. The interface with cCeO₂-NO₃ exhibits the highest affinity to the SiO₂ surface, with a W_{ad}

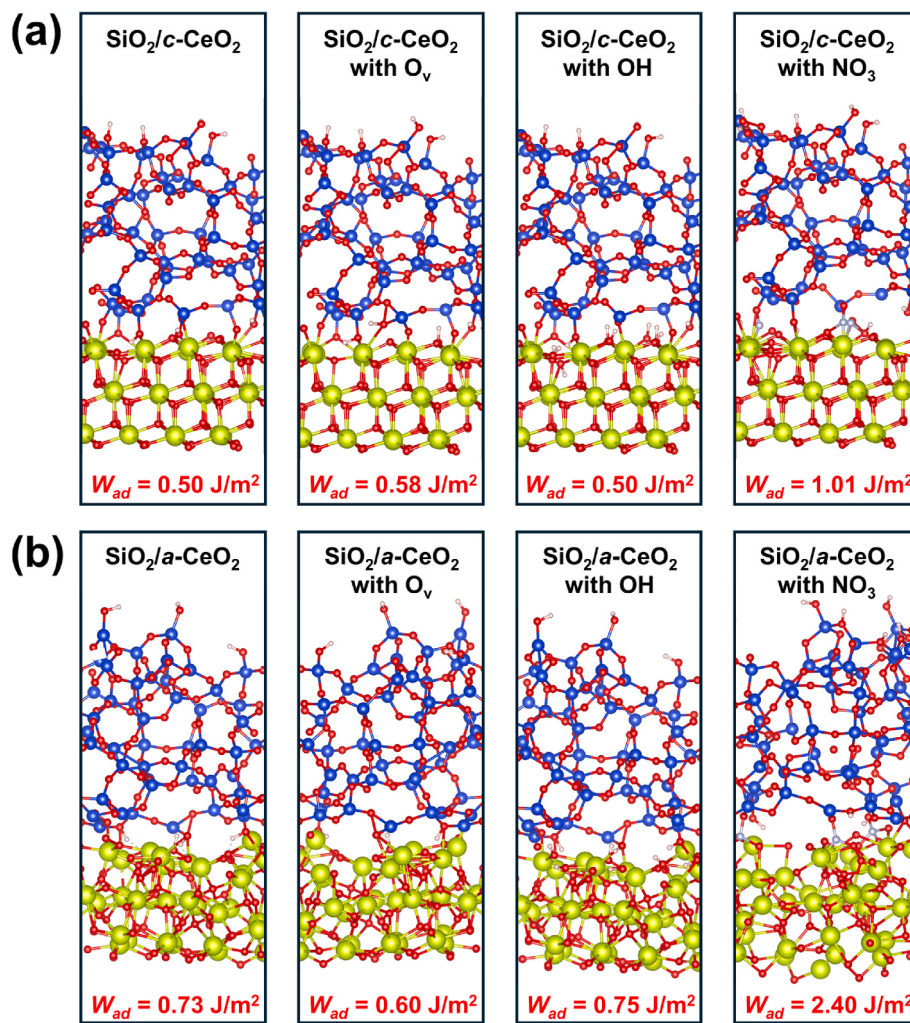


Fig. 7. Simulation models depicting the work of adhesion (W_{ad}) between CeO_2 and SiO_2 , showcasing two different scenarios: (a) with crystalline CeO_2 and (b) with amorphous CeO_2 . Both models include O_L , O_v , $-\text{OH}$ groups, and $-\text{NO}_3$ groups. In these models, green spheres represent Ce^{4+} ions, blue spheres depict Si^{4+} ions, red spheres are used to indicate O^{2-} ions, and silver spheres denote N ions. (For interpretation of the references to color in this figure legend, the reader is referred to the Web version of this article.)

value of 1.01 J/m^2 .

Conversely, W_{ad} values at the $\text{SiO}_2/\text{aCeO}_2\text{-O}_L$ and $\text{aCeO}_2\text{-OH}$ interfaces were recorded at 0.73 J/m^2 and 0.75 J/m^2 , respectively, indicating that the amorphous structure's increased surface reactivity significantly strengthens the interface. The introduction of O_v decreases these values to 0.60 J/m^2 . Among the materials studied, $\text{aCeO}_2\text{-NO}_3$ exhibits the highest affinity towards the SiO_2 surface, with a W_{ad} of 2.40 J/m^2 .

When the particles exhibit high crystallinity, Ce^{3+} sites ($\text{cCeO}_2\text{-O}_v$) show elevated W_{ad} values for SiO_2 , which correlates with the role of Ce^{3+} as active sites for enhancing SiO_2 removal rates. Although we did not detect the NO_3 group in our highly crystalline CeO_2 derived by Ce^{3+} precursors (Fig. 4 and Table 2), modifying CeO_2 particles with NO_3 groups could potentially increase their affinity for SiO_2 , thereby improving the SiO_2 film removal rate. Interestingly, our DFT simulations reveal that Ce^{3+} sites ($\text{aCeO}_2\text{-O}_v$) have the lowest work of adhesion, suggesting these may not be active sites in amorphous regions. In contrast, our less crystalline CeO_2 particles derived from Ce^{4+} precursors contain higher concentrations of $-\text{OH}$ and $-\text{NO}_3$ groups (Fig. 4 and Table 2) and exhibit higher W_{ad} values. These groups are likely the active sites in low crystalline CeO_2 particles for SiO_2 CMP. It is important to note that overall bonds between SiO_2 and aCeO_2 are much stronger than those with cCeO_2 . The highly reactive surface of the amorphous

regions might explain the increased efficiency of CMP processes using low crystalline CeO_2 particles, which have high densities of OH and NO_3 groups on their surface. Consequently, low crystalline ceria could lead to more effective SiO_2 removal in CMP applications due to its stronger interactions with SiO_2 films.

4. Conclusions

In conclusion, we demonstrated the profound impact of Ce precursors (Ce^{3+} and Ce^{4+}), Ce/OH molar ratios, and reaction temperatures on the physicochemical properties of superfine CeO_2 particles. Our XRD results clearly show that superfine ceria particles derived from the Ce^{3+} precursor ($\text{Ce}(\text{NO}_3)_3$) have larger crystallite sizes and higher crystallinity compared to those synthesized from the Ce^{4+} precursor ($(\text{NH}_4)_2\text{Ce}(\text{NO}_3)_6$). This difference is attributed to their reaction pathways and solubility characteristics of the precursors, which significantly influence the nucleation and growth processes of the CeO_2 particles.

Surprisingly, the Ce^{4+} -derived particles, with their smaller size (around 5 nm), demonstrated superior SiO_2 film removal rates compared to the larger Ce^{3+} -derived particles. This finding emphasizes the role of chemical action in the CMP process, challenging the traditional belief that larger particles primarily drive higher removal rates due to mechanical abrasion.

FT-IR and TGA analyses further reveal distinct surface chemistry profiles between the Ce³⁺ and Ce⁴⁺-derived ceria particles. The presence and density of various functional groups on the particle surfaces, as evidenced by CHN analysis, show different adsorption behaviors. Particularly, Ce⁴⁺-derived particles exhibit a higher adsorption capacity for NO₃ species, likely due to their lower crystallinity and the increased number of surface acidic sites. Notably, Ce⁴⁺-derived particles demonstrate a higher weight loss of 11 % compared to 3 % in Ce³⁺-derived particles, indicative of their distinct surface functional group compositions. The Ce⁴⁺-derived particles contain 0.65 % C, 0.62 % H, and 1.34 % N, with a higher density of OH groups (24.08 nm²) and the presence of NO₃ groups (3.72 nm²), compared to Ce³⁺-derived particles which contain 0.61 % C and 0.23 % H, with a lower OH group density (15.91 nm²).

Through detailed theoretical and DFT analyses, we have shown that the nature and concentration of CeO₂ functional groups, derived from both Ce³⁺ and Ce⁴⁺ precursors, critically impact the work of adhesion with SiO₂. Our results distinctly reveal that *a*CeO₂ surfaces generally exhibit higher W_{ad} values with SiO₂ compared to their *c*CeO₂. Specifically, W_{ad} values for SiO₂/*a*CeO₂-OL and *a*CeO₂-OH interfaces were 0.73 J/m² and 0.75 J/m², respectively, compared to 0.50 J/m² for *c*CeO₂-OL and -OH groups. The introduction of O_v revealed divergent effects: increasing W_{ad} for crystalline CeO₂/SiO₂ (0.58 J/m²) while decreasing it for *a*CeO₂/SiO₂ (0.60 J/m²). Notably, *a*CeO₂-NO₃ showed the highest SiO₂ affinity with a W_{ad} of 2.40 J/m². Our results demonstrated that less *c*CeO₂, rich in -OH and -NO₃ groups, showed higher adhesion energies, suggesting their greater efficacy in CMP processes. This study highlights the importance of the surface chemistry of CeO₂ particles and crystallinity in semiconductor fabrication, offering insights for developing next-generation abrasives for CMP applications.

Data and code availability

Data is available upon request.

CRediT authorship contribution statement

Ravitej Venkataswamy: Writing – review & editing, Writing – original draft, Visualization, Validation, Resources, Methodology, Investigation, Formal analysis, Data curation. **Lyle Trimble:** Methodology, Investigation, Formal analysis, Data curation. **Seokgyu Ryu:** Writing – original draft, Visualization, Validation, Software, Investigation, Data curation. **Ngoc-Tram Le:** Methodology, Investigation, Formal analysis, Data curation. **Kyungju Park:** Writing – review & editing, Visualization, Supervision, Project administration, Funding acquisition, Conceptualization. **Hyungoo Kang:** Writing – review & editing, Supervision, Resources, Project administration, Funding acquisition, Conceptualization. **Jihoon Seo:** Writing – review & editing, Writing – original draft, Visualization, Validation, Supervision, Project administration, Methodology, Investigation, Funding acquisition, Formal analysis, Data curation, Conceptualization.

Declaration of competing interest

The authors declare that they have no known competing financial interests or personal relationships that could have appeared to influence the work reported in this paper.

Acknowledgment

We gratefully acknowledge SK Hynix for providing partial financial support.

Appendix A. Supplementary data

Supplementary data to this article can be found online at <https://doi.org/10.1016/j.ceramint.2024.08.444>.

<https://doi.org/10.1016/j.ceramint.2024.08.444>

References

- [1] O. Burkacky, J. Dragon, N. Lehmann, The Semiconductor Decade: A Trillion-Dollar Industry, vol. 1, McKinsey & Company, 2022.
- [2] W.M. Arden, The international technology roadmap for semiconductors—perspectives and challenges for the next 15 years, *Curr. Opin. Solid State Mater. Sci.* 6 (2002) 371–377.
- [3] S. Babu, Advances in Chemical Mechanical Planarization (CMP), Woodhead Publishing, 2021.
- [4] J. Seo, A review on chemical and mechanical phenomena at the wafer interface during chemical mechanical planarization, *J. Mater. Res.* 36 (2021) 235–257.
- [5] D. Datta, H. Rai, S. Singh, M. Srivastava, R.K. Sharma, N.N. Gosvami, Nanoscale tribological aspects of chemical mechanical polishing: a review, *Appl. Surface Sci. Adv.* 11 (2022) 100286.
- [6] R. Srinivasan, P.V. Dandu, S. Babu, Shallow trench isolation chemical mechanical planarization: a review, *ECS J. Solid State Sci. Technol.* 4 (2015) P5029.
- [7] J. Seo, J.W. Lee, J. Moon, W. Sigmund, U. Paik, Role of the surface chemistry of ceria surfaces on silicate adsorption, *ACS Appl. Mater. Interfaces* 6 (2014) 7388–7394.
- [8] C. Chen, Y. Cui, X. Li, S. Shen, W. Liao, H. You, Novel ceria/graphene oxide composite abrasives for chemical mechanical polishing, *Ceram. Int.* (2024).
- [9] A. Othman, A. Gowda, D. Andreescu, M.H. Hassan, S. Babu, J. Seo, D. Andreescu, Two decades of ceria nanoparticles research: structure, properties and emerging applications, *Mater. Horiz.* (2024).
- [10] J. Seo, K. Kim, H. Kang, S. Babu, Perspective—recent advances and thoughts on Ceria particle applications in chemical mechanical planarization, *ECS J. Solid State Sci. Technol.* (2022).
- [11] T. Iwano, H. Akimoto, T. Narita, T. Kimura, D. Ryuzaki, Slurry, Polishing Fluid Set, Polishing Fluid, and Substrate Polishing Method Using Same, Resonac Corp, USA, 2018.
- [12] Y.-H. Son, G.-P. Jeong, P.-S. Kim, M.-H. Han, S.-W. Hong, J.-Y. Bae, S.-I. Kim, J.-H. Park, J.-G. Park, Super fine cerium hydroxide abrasives for SiO₂ film chemical mechanical planarization performing scratch free, *Sci. Rep.* 11 (2021) 17736.
- [13] Y. Xu, S.S. Mofarah, R. Mehmood, C. Cazorla, P. Koshy, C.C. Sorrell, Design strategies for ceria nanomaterials: untangling key mechanistic concepts, *Mater. Horiz.* 8 (2021) 102–123.
- [14] R. Wang, R. Dangerfield, Seed-mediated synthesis of shape-controlled CeO₂ nanocrystals, *RSC Adv.* 4 (2014) 3615–3620.
- [15] G. Kresse, J. Furthmüller, VASP—the guide (Universität wien, wien, Austria, 2007); G. Kresse and J. Hafner, *Phys. Rev. B* 47 (1993) 558.
- [16] V.I. Anisimov, J. Zaanen, O.K. Andersen, Band theory and Mott insulators: Hubbard U instead of Stoner I, *Phys. Rev. B* 44 (1991) 943.
- [17] S. Grimme, Semiempirical GGA-type density functional constructed with a long-range dispersion correction, *J. Comput. Chem.* 27 (2006) 1787–1799.
- [18] H.J. Monkhorst, J.D. Pack, Special points for Brillouin-zone integrations, *Phys. Rev. B* 13 (1976) 5188.
- [19] S. Karthika, T. Radhakrishnan, P. Kalaichelvi, A review of classical and nonclassical nucleation theories, *Cryst. Growth Des.* 16 (2016) 6663–6681.
- [20] Z. Wu, S. Yang, W. Wu, Shape control of inorganic nanoparticles from solution, *Nanoscale* 8 (2016) 1237–1259.
- [21] S.G. Kwon, T. Hyeon, Formation mechanisms of uniform nanocrystals via hot-injection and heat-up methods, *Small* 7 (2011) 2685–2702.
- [22] J.A. Dean, Lange's Handbook of Chemistry, Citeseer, 1999.
- [23] J.-S. Lee, S.-C. Choi, Crystallization behavior of nano-ceria powders by hydrothermal synthesis using a mixture of H₂O₂ and NH₄OH, *Mater. Lett.* 58 (2004) 390–393.
- [24] J.-K. Lai, N.R. Jaegers, B.M. Lis, M. Guo, M.E. Ford, E. Walter, Y. Wang, J.Z. Hu, I. E. Wachs, Structure–activity relationships of hydrothermally aged Titania-Supported Vanadium-Tungsten oxide catalysts for SCR of NO_x emissions with NH₃, *ACS Catal.* 11 (2021) 12096–12111.
- [25] Y. Wang, F. Wang, Q. Song, Q. Xin, S. Xu, J. Xu, Heterogeneous ceria catalyst with water-tolerant Lewis acidic sites for one-pot synthesis of 1, 3-diols via Prins condensation and hydrolysis reactions, *J. Am. Chem. Soc.* 135 (2013) 1506–1515.
- [26] Z. Wu, A.K. Mann, M. Li, S.H. Overbury, Spectroscopic investigation of surface-dependent acid–base property of ceria nanoshapes, *J. Phys. Chem. C* 119 (2015) 7340–7350.
- [27] M. Nabavi, O. Spalla, B. Cabane, Surface chemistry of nanometric ceria particles in aqueous dispersions, *J. Colloid Interface Sci.* 160 (1993) 459–471.
- [28] A. Koutsianos, A.R. Barron, E. Andreoli, CO₂ capture partner molecules in highly loaded PEI sorbents, *J. Phys. Chem. C* 121 (2017) 21772–21781.
- [29] X. Shi, J. Du, T.G. Jones, X. Wang, H.-P. Liang, Understanding the mechanism for capacity Decay of V6O13-based Lithium-metal Polymer Batteries, *ACS Appl. Mater. Interfaces* 10 (2018) 29667–29674.
- [30] F. Cataldo, O. Ursini, C. Cherubini, S. Rocchi, Synthesis of *cis*-and *trans*-polysoprene adduct with nitrogen dioxide (NO₂/N₂O₄ mixture) and a study of the thermal stability of the adduct, *Polym. Degrad. Stabil.* 97 (2012) 1090–1100.
- [31] M. Jin, N. Luo, G. Li, Y. Luo, The thermal decomposition mechanism of nitrocellulose aerogel, *J. Therm. Anal. Calorim.* 121 (2015) 901–908.
- [32] Z. Li, L. Jin, Z. Cao, C. Zhang, X. Cao, G. Han, S. Peng, Y. Liu, Development and characterization of a novel RE3+ doped Core-shell CeO₂ abrasive system and its glass CMP investigations, *Appl. Surf. Sci.* 638 (2023) 158055.

- [33] X. Yuan, H. Lei, C. Chen, An ethylenediaminetetraacetic acid (EDTA) surface-functionalized CeO₂ composite abrasives with the effective improvement of the removal rate on glass CMP, *Ceram. Int.* 50 (2024) 293–305.
- [34] A. Chen, S. Wang, J. Pan, T. Wang, Y. Chen, Development of Zr-and Gd-doped porous ceria (pCeO₂) abrasives for achieving high-quality and high-efficiency oxide chemical mechanical polishing, *Ceram. Int.* 48 (2022) 14039–14049.
- [35] D. Jampaiah, K.M. Tur, S.J. Ippolito, Y.M. Sabri, J. Tardio, S.K. Bhargava, B. M. Reddy, Structural characterization and catalytic evaluation of transition and rare earth metal doped ceria-based solid solutions for elemental mercury oxidation, *RSC Adv.* 3 (2013) 12963–12974.
- [36] S. Park, J. Seo, Comparative first-principles analysis of crystalline versus amorphous CeO₂ particles: implications for chemical mechanical planarization, *J. Mater. Sci.* (2024) 1–11.
- [37] O. Kraynis, I. Lubomirsky, T. Livneh, Resonant Raman scattering in undoped and lanthanide-doped CeO₂, *J. Phys. Chem. C* 123 (2019) 24111–24117.
- [38] T. Vinodkumar, D.N. Durgasri, S. Maloth, B.M. Reddy, Tuning the structural and catalytic properties of ceria by doping with Zr 4+, La 3+ and Eu 3+ cations, *J. Chem. Sci.* 127 (2015) 1145–1153.
- [39] H. Kanno, J. Hiraishi, Raman study of aqueous rare earth nitrate solutions in liquid and glassy states, *J. Phys. Chem.* 88 (1984) 2787–2792.
- [40] G. Zhang, Z. Shen, M. Liu, C. Guo, P. Sun, Z. Yuan, B. Li, D. Ding, T. Chen, Synthesis and characterization of mesoporous ceria with hierarchical nanoarchitecture controlled by amino acids, *J. Phys. Chem. B* 110 (2006) 25782–25790.
- [41] M. Piumetti, S. Bensaid, N. Russo, D. Fino, Nanostructured ceria-based catalysts for soot combustion: investigations on the surface sensitivity, *Appl. Catal. B Environ.* 165 (2015) 742–751.
- [42] D. Mullins, S. Overbury, D. Huntley, Electron spectroscopy of single crystal and polycrystalline cerium oxide surfaces, *Surf. Sci.* 409 (1998) 307–319.
- [43] T. Hasegawa, S.M.F. Shahed, Y. Sainoo, A. Beniya, N. Isomura, Y. Watanabe, T. Komeda, Epitaxial growth of CeO₂ (111) film on Ru (0001): Scanning tunneling microscopy (STM) and x-ray photoemission spectroscopy (XPS) study, *J. Chem. Phys.* 140 (2014).
- [44] L. Kundakovic, D. Mullins, S. Overbury, Adsorption and reaction of H₂O and CO on oxidized and reduced Rh/CeO_x (111) surfaces, *Surf. Sci.* 457 (2000) 51–62.
- [45] M.A. Henderson, C. Perkins, M.H. Engelhard, S. Thevuthasan, C.H. Peden, Redox properties of water on the oxidized and reduced surfaces of CeO₂ (111), *Surf. Sci.* 526 (2003) 1–18.
- [46] Y. Peng, W. Si, J. Luo, W. Su, H. Chang, J. Li, J. Hao, J. Crittenden, Surface tuning of La_{0.55}Sr_{0.5}CoO₃ perovskite catalysts by acetic acid for NO_x storage and reduction, *Environ. Sci. Technol.* 50 (2016) 6442–6448.